Pseudodielectric function and critical-point energies of iron pyrite

S. G. Choi,[1,*] J. Hu,[2] L. S. Abdallah,[3] M. Limpinsel,[4] Y. N. Zhang,[2] S. Zollner,[3] R. Q. Wu,[2] and M. Law[4]

[1]*National Renewable Energy Laboratory, Golden, Colorado 80401, USA*

[2]*Department of Physics and Astronomy, University of California, Irvine, California 92697, USA*

[3]*Department of Physics, New Mexico State University, Las Cruces, New Mexico 88003, USA*

[4]*Department of Chemistry, University of California, Irvine, California 92697, USA*

Spectroscopic ellipsometry was used to determine the pseudodielectric function $\langle\varepsilon\rangle = \langle\varepsilon_1\rangle + i\langle\varepsilon_2\rangle$ spectrum of a natural single crystal of iron pyrite (cubic FeS_2) from 0.5 to 4.5 eV with the sample at 77 K. The $\langle\varepsilon\rangle$ spectrum exhibits several pronounced optical features associated with the interband critical points (CPs). Accurate CP energies are obtained by fitting standard line shapes to second energy derivatives of the $\langle\varepsilon\rangle$ data. The electronic origins of the six observed CP features are identified through density functional theory calculations and momentum matrix analyses.

I. INTRODUCTION

Iron pyrite (FeS_2) has long been considered a promising absorber material for thin-film photovoltaics (PVs).[1] Pyrite is reported to possess a band gap of ∼0.95 eV at room temperature, which is suitable for the effective harvesting of solar energy. Its high absorption coefficient ($\alpha > 10^5$ cm^{-1} for $E > 1.3$ eV) leads to excellent quantum efficiencies (>90%) and large photocurrents (>40 mA/cm^2) in single crystals.[2] In addition, the vast abundance and low procurement cost of the constituent elements may make pyrite PV a practical solution for terawatt-scale solar electricity generation.[3]

The complex dielectric function $\varepsilon = \varepsilon_1 + i\varepsilon_2$ and complex refractive index $N = n + ik$ are important for understanding the electronic structure of materials[4] and developing PV device structures.[5] However, only a limited number of ε and N spectra are available for pyrite from electronic structure calculations[6–9] or optical reflectance measurements.[10–13] Moreover, significant discrepancies exist among the reported spectra, and no trustworthy theoretical explanation has been made available so far.

Here, we report the *pseudodielectric function* $\langle\varepsilon\rangle$ spectrum of a natural pyrite single crystal as determined by spectroscopic ellipsometry (SE) at 77 K. SE determines ε and N spectra without use of the Kramers-Kronig transform and is known to be more accurate than conventional reflectance techniques.[14] Our SE spectrum reveals several above-band-gap optical structures associated with interband critical points (CPs)[15] that correspond to Van Hove singularities in the joint density of states (JDOS) $D_j(E_{cv})$, defined as

$$D_j(E_{cv}) = \frac{1}{4\pi^3} \int \frac{dS_k}{|\nabla_k[E_{cv}(\vec{k})]|}. \tag{1}$$

Here, S_k is the constant energy surface in reciprocal space defined by $E_{cv}(\vec{k}) \equiv E_c(\vec{k}) - E_v(\vec{k}) = \hbar\omega$. The major optical feature occurs at the CP in reciprocal space, where $|\nabla_k E_{cv}(\vec{k}) = 0|$.

We obtain accurate CP energies by fitting standard line shapes to second derivatives of the $\langle\varepsilon(E)\rangle$ data[16,17] and identify

their electronic origin by comparing the experimental data to the results of density functional theory (DFT) calculations.

II. EXPERIMENTS

A natural pyrite single crystal from Erzurum, Turkey, sectioned along the (111) surface, was used in this study. For resistivity and Hall effect measurements, ohmic contacts were made to polished slices of the crystal using 40-nm-thick evaporated gold pads covered in dots of colloidal silver paste. The measurements were performed using the van der Pauw method with a magnetic field of 0.55 T and a current of 20 mA. The room-temperature carrier concentration, mobility, and resistivity of this *n*-type crystal were 1×10^{18} cm^{-3}, 75 cm^2/V·s, and 0.083 Ω cm, respectively [Figs. 1(c) and 1(d)]. These values are typical of relatively highly doped natural pyrite crystals.

Since SE measurements are often influenced by surface overlayer artifacts such as microscopic roughness, native oxides, and hydrocarbon contamination,[18] we reduced the surface roughness by chemical mechanical polishing of the crystal. After successive grinding steps with abrasive SiC paper and polishing with a diamond particle suspension, the final polishing step employed a colloidal silica suspension with a particle size of 50 nm. Possible silica residue on the surface from the final polishing step was etched away by concentrated hydrofluoric acid (48%) followed by a deionized water rinse. Finally, the crystal was sonicated in methanol. The resulting rms roughness was estimated by atomic force microscopy (AFM) to be 2 to 3 nm over $20 \times 20 \ \mu m^2$ areas [Fig. 1(b)]. An x-ray diffraction pattern of a powdered piece of this crystal shows no evidence for any phases other than pyrite [Fig. 1(a)].

SE data were acquired from 0.5 to 4.5 eV with a step size that was 0.01 eV at 77 K using a rotating analyzer-type ellipsometer equipped with a computer-controlled Berek wave-plate compensator [J. A. Woollam Inc., variable-angle spectroscopic ellipsometry (VASE) system]. The sample temperature was adjusted by a liquid-nitrogen-cooled variable-temperature cryostat. The angle of incidence was 70°. To increase the signal-to-noise ratio, each data point was recorded

after averaging 100 analyzer cycles (100 revolutions per measurement).

III. DENSITY FUNCTIONAL PERTURBATION THEORY CALCULATIONS

To elucidate the electronic origin of each CP structure, we carried out spin-polarized density functional calculations with the Vienna *Ab initio* Simulation Package (VASP),[20,21] at the level of the generalized gradient approximation (GGA).[22] The projector augmented wave (PAW) method was adopted for the description of the core-valence interaction.[23,24] The experimental lattice constant ($a = 5.418$ Å) was used in this work, which is, nonetheless, very close to the optimized lattice size ($a = 5.403$ Å). We set an energy cutoff of 350 eV for the basis expansion and used a $13 \times 13 \times 13$ k-grid mesh to sample the Brillouin zone.[25] The pyrite FeS_2 structure is similar to rocksalt ($Pa\bar{3}$ space group)[26] and features interpenetrating face-centered cubic sublattices of Fe^{2+} ions and S_2^{2-} dimers pointed along the $\langle 111 \rangle$ directions. Each Fe atom has an octahedral coordination to six S atoms, and each S atom has three Fe neighbors and one S neighbor. The octahedral crystal field causes splitting of the $3d$ orbitals of Fe atom into two groups, t_{2g} (d_{xy}, d_{xz}, and d_{yz}) and e_g (d_{z2} and d_{x2-y2}), which constitute the valence and conduction bands, respectively.[8,27] Three t_{2g} states are fully occupied by six $3d$ electrons of Fe^{2+} cations, which results in a nonmagnetic ground state of pyrite FeS_2.[28] On the other hand, the conduction bands are mixtures of Fe e_g and S $pp\sigma^*$ states, so they also comprise $l = 1$ components around the Fe atoms, which is crucial for efficient optical absorption.

Within the electric dipole approximation, $\varepsilon(E)$ can be directly calculated using density functional perturbation theory[29] as (in atomic units):

$$\varepsilon_{xx}(E) = 1 + \frac{4\pi}{\Omega E} \sum_{\vec{k}} \sum_{mn} \frac{f_m - f_n}{E_{mn}} \cdot \frac{|p_{x,mn}(\vec{k})|^2}{E - E_{mn} + i\delta}. \quad (2)$$

Here, Ω is the volume of the pyrite cell, δ is a broadening width ($\delta = 0.1$ eV in the present work), E is the incident photon energy, $\vec{k}$ is the wave vector in the Brillouin zone (BZ), f_m is the electron occupancy of the mth eigenstate, E_{mn} is the energy difference between the mth and nth states, and $p_{x,nm}$ is the matrix element of the x component of momentum operator. For a cubic crystal such as pyrite, we have $\varepsilon_{xx} = \varepsilon_{yy} = \varepsilon_{zz} = \varepsilon$.

IV. RESULTS AND DISCUSSION

The SE-determined $\langle \varepsilon \rangle$ spectrum of the natural pyrite crystal and the calculated ε curve are shown in Fig. 2. Two prominent CP features are evident in the SE data at ~2.0 and ~4.0 eV, as also observed in early studies.[8–13] Although the calculations slightly overestimate the CP energies below 3 eV and underestimate those above it, the overall agreement between experimental and theoretical results is obvious. All six of the major CP features observed experimentally are captured in the DFT calculations. The calculated value of the static dielectric constant ($\varepsilon_\infty = 21$) is also consistent with the experimental data. Although noticeable differences in
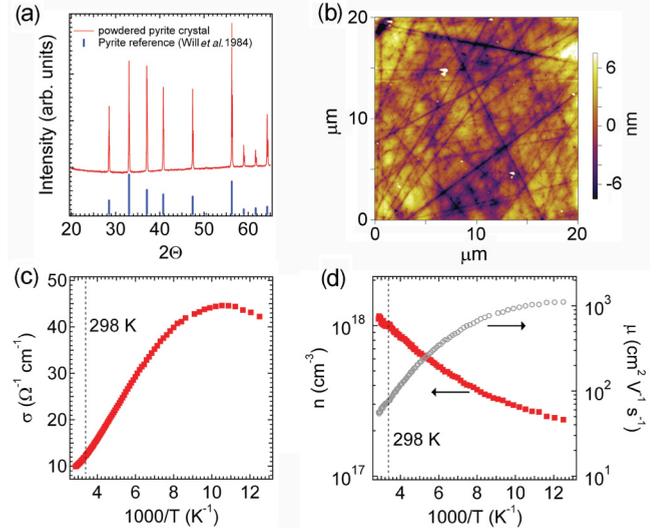
FIG. 1. (Color online) (a) X-ray diffraction pattern of a powdered slice of the crystal, showing phase-pure pyrite, along with a pyrite reference pattern.[19] (b) AFM topography scan (ac mode), showing a 20×20 μm area of the polished crystal with 2.8-nm rms roughness. (c) Temperature-dependent conductivity and (d) carrier concentration and mobility from 80 to 350 K determined by Hall effect measurements.

peak height ratios still exist due to the omission of high-level many-body corrections such as GW[30] and time-dependent density functional theory,[31] the present GGA level calculations appear to be adequate for assigning the electronic origins of the optical features.

Although the band-gap energy of pyrite is thought to be ~0.95 eV,[1,2] our SE data show nonzero $\langle \varepsilon_2 \rangle$ values below the band gap rather than an abrupt fundamental absorption edge. This is probably due in part to lifetime broadening and also the presence of native oxides on the crystal surface as well as the nanometer-scale surface roughness.[18] Lifetime
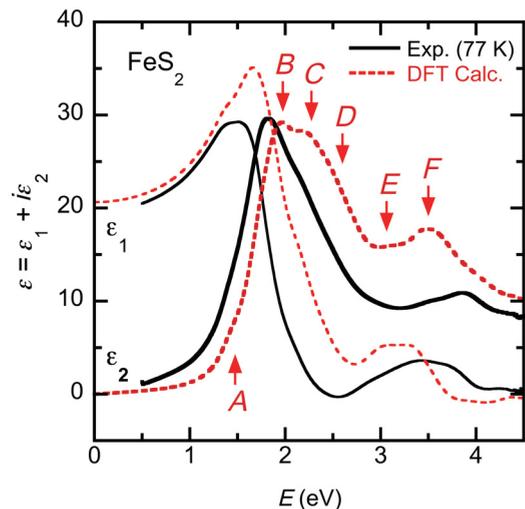
FIG. 2. (Color online) Experimental (solid black lines) and calculated (dashed red lines) ε spectra for a pyrite crystal. The experimental data were taken at 77 K. The major CP features seen in the calculated ε_2 spectrum are labeled alphabetically.
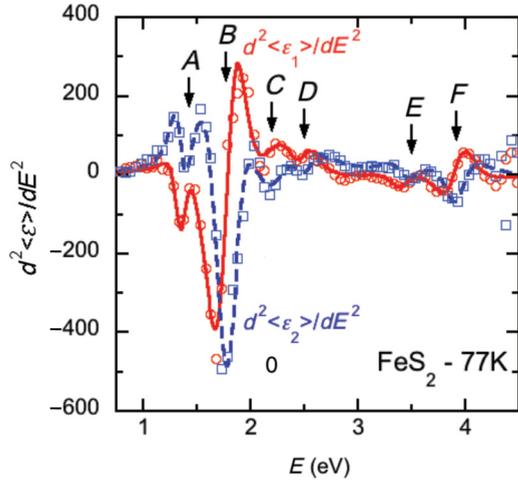
FIG. 3. (Color online) Best fits to the second derivatives of $\langle \varepsilon_1 \rangle$ (solid red line) and $\langle \varepsilon \rangle$ (dashed blue line). The red circles and blue squares are numerical calculations of $d^2\langle \varepsilon_1 \rangle / dE^2$ and $d^2\langle \varepsilon_2 \rangle / dE^2$, respectively. For clarity, only one-fifth of the data points are shown. The line shapes used to fit the data are labeled in accordance with Fig. 2.

broadening due to lattice vibrations causes absorption below the band gap, which is similar to band tails in amorphous semiconductors.[17] Oxidation of pyrite surfaces can be very rapid,[32] and the formation of surface oxides was inevitable during sample preparation. Since the exact thickness and chemical characteristics of native oxides on pyrite are not known *a priori*, we did not attempt a multilayer analysis in this study. A multilayer analysis with very limited information potentially leads to inaccurate results. Another possible cause of the nonzero absorption below 0.95 eV includes surface and bulk defects that may induce states within the band gap.[33]

The energies of the CP features observed in our SE data are accurately obtained by fitting the standard analytic CP expressions[34,35] to second energy derivatives of the $\langle \varepsilon \rangle$ data calculated numerically from linear filtering algorithms of the Savitzky-Golay type.[36] The CP expressions are

$$\frac{d^2\varepsilon}{dE^2} = \begin{cases} n(n-1)Ae^{i\phi}(E - E_g + i\Gamma)^{n-2}, & n \neq 0 \\ Ae^{i\phi}(E - E_g + i\Gamma)^{-2}, & n = 0 \end{cases}, \quad (3)$$

where A is the amplitude, E_g is the threshold energy, Γ is the broadening parameter, and ϕ is the phase. The exponent n has values of -1, $-\frac{1}{2}$, 0, and $\frac{1}{2}$ for excitonic, one-, two-, and three-dimensional line shapes, respectively. The real and imaginary parts were fit simultaneously.

The $d^2\langle \varepsilon \rangle / dE^2$ spectrum together with the best-fit curves are shown as open symbols and lines, respectively, in Fig. 3. A total of six excitonic ($n = -1$) line shapes[4,17,37–39] are used to fit the data from 1 to 4.5 eV, which resulted in the lowest mean-square deviation. Each peak is identified in accordance with Fig. 2. Several weak CPs (A, C, D, and E), clearly resolved in the derivative spectrum, have not been previously discussed in the literature.[6–13] The fit-determined CP energies are listed in Table I. The energy values reported in previous studies[6–9,11,12] as well as our DFT results (discussed below) are also included for comparison. The broadening parameters Γ for the A, B, C, D, E, and F CPs, obtained by the

TABLE I. CP energies (in eV) for pyrite. Previously reported CP energies are included for comparison.

CP		A	B	C	D	E	F
This work	Exp.	1.36	1.78	2.09	2.49	3.41	3.92
	Theory	1.30	1.96	2.27	2.60	3.10	3.50
Ref. 6			2.00				
Ref. 7			2.10				3.30
Ref. 8			2.10				3.50
Ref. 9			2.00				3.60
Ref. 11			1.70		2.30		3.80
Ref. 12			1.6				4

line-shape analysis, are 131, 255, 542, 184, 239, and 248 meV, respectively. However, one needs to be cautious to interpret these broadening parameters and line shapes, due to the complexities of band structures of pyrite.

It is known that the optical absorption spectrum of pyrite results from electric dipole transitions from the Fe t_{2g} states in the valence bands (VBs) to the Fe e_g and S-S $pp\sigma^*$ mixtures in the conduction bands.[8,27] However, the key states related to these transitions and their distribution in the BZ have not been clearly identified. According to Eq. (2), contributions to ε from states m and n depend on the square of the momentum matrix element $|p_{x,mn}(\vec{k})|^2$ and their energy difference E_{mn}. By analyzing this matrix element in a narrow energy window over the entire BZ, we can identify the initial and final electronic states across which the electric dipole transitions contribute the most to each CP. Results of these analyses are displayed in Figs. 4(a) and 4(b), along with the calculated band structure of pyrite.

First, it is interesting to note that the magnitude of $|p_{x,mn}(\vec{k})|^2$ for optical transitions from VBs to the conduction-band minimum (CBM) near the center of BZ is negligible, since CBM associates rather purely with S $pp\sigma^*$ orbitals, whereas VB states mostly localize around the Fe atoms. As a result, the optical absorption edge of iron pyrite starts much higher than the band gap. The main absorption features, i.e., the B CP at 2.0 eV and the C CP at 2.3 eV in the calculated ε_2 curve (dashed red) in Fig. 2, originate from transitions between orbital of Fe atoms. To better appreciate this, we plot in Fig. 4(b) the isosurface of $|p_{x,mn}(\vec{k})|^2$ in the BZ and its two-dimensional contour map at $k_z = \pi/a$ for the B CP with $E_{mn} = 2.0 \pm 0.1$ eV. Clearly, the main contributions to the B CP are from electric dipole transitions in the vicinity of the M points in the BZ. The initial and final states that are responsible for the B CP are the occupied Fe t_{2g} state and hybridized Fe e_g and S-S $pp\sigma^*$ state as depicted in Fig. 4(a). The C CP can be assigned to transitions near the X point, along with a relatively weak transition at the M point, as shown Fig. 4(a). We note that the C CP and its origin have not been identified in previous theoretical studies.[6–9]

This procedure was applied to all CPs, and arrows in Fig. 4(a) show the key pairs of states and their locations in the BZ. The second major CP feature F from DFT lies at ~3.5 eV, which is ~0.3 eV lower than the corresponding experimental value. The transitions associated with this CP occur near the M, Γ, and R points in the BZ, with both the initial and final
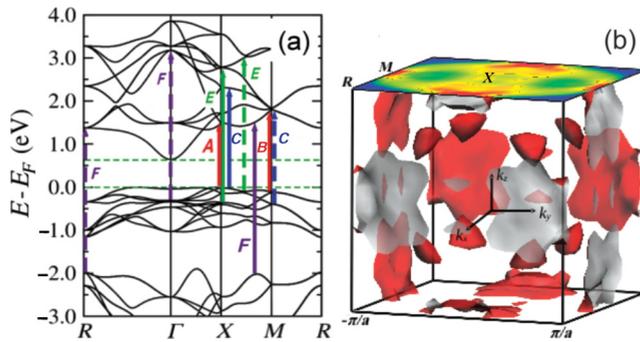
FIG. 4. (Color online) (a) Band structure of bulk pyrite, with arrows denoting the main transitions associated with the CPs labeled in Fig. 2. (b) The isosurface of $|p_{x,mn}(\vec{k})|^2$ in the Brillouin zone for the *B* CP. A two-dimensional contour is also shown for $k_z = \pi/a$ (*a* is the lattice constant of pyrite).

states a mixture of Fe 3*d* and S 3*p* orbitals. Our momentum matrix analyses suggest that the transition occurring near the *M* point is the dominant contribution to *F*. Our assignments for the *B* and *F* CPs are similar to those of Lauer *et al.*[6] and Antonov *et al.*[8]

We note that different explanations for the origin of features *B* and *F* have been reported. Based on the results from their full-potential linearized-augmented plane-wave calculations, Vadkhiya *et al.*[9] assigned the *B* and *F* CPs to the transitions from Fe 3*d* to S 3*p* states at the *R* point and *X* point, respectively. However, in our calculation, the momentum matrices related these transitions are almost zero, due to the very small overlap between the Fe t_{2g} and S $pp\sigma^*$ orbitals. Schlegel *et al.*[11] related the structure at $\sim$2 eV (*B* CP) to 3*d* *intraband* transitions from t_{2g} states to antibonding e_g^* states, and the high-energy structures (*F* CP) to *interband* transitions from states of largely S 3*p* character into Fe e_g^* states. These assignments appear to be arbitrary and do not agree with our results in Fig. 4(a).

Among the minor peaks that have not been discussed in previous studies,[6–13] the *A* CP at $\sim$1.5 eV is crucial for applications of pyrite in PV since it is the first major absorption feature above the band gap. It results from the transition between the Fe t_{2g} state at the valence-band maximum and the mixed Fe-S state (Fe e_g + S $pp\sigma^*$) near the *X* point. The *plateau-like E* CP at $\sim$3 eV is composed of a series of transitions from the Fe t_{2g} states to hybridized states of Fe e_g and S $pp\sigma^*$ along the *X*-*M* direction in the BZ. Finally, the *D* CP results mainly from transitions in the wide region near the *M* points, and contributions from other *k*-points are also substantial. Therefore, we chose not to denote the transitions responsible for this CP in Fig. 4(a).

We want to point out that most CPs, in particular the *C* and *E* CPs, contain multiple contributions from different parts of BZ. This makes the assignments of dimensionality and type of symmetry of their corresponding Van Hove singularities impractical. Nevertheless, we may still roughly trace their origins from the band structure in Fig. 4. For example, the *B* CP shows a two-dimensional saddle-point feature in the *MRM* plane, whereas the *F* CP appears to be a three-dimensional M_0 singularity.

In order to obtain the better band gap, the Hubbard correction was typically included in recent density functional calculations for iron pyrite (e.g., $U = 2.0$ eV for the Fe 3*d* orbitals).[27] We found, however, that it significantly worsens the agreement of optical spectrum by shifting most CPs upward by 0.3–0.5 eV. On the other hand, the GW correction reduces the band gap to 0.4 eV but does not much affect the optical functions. Also, an unreasonably large band gap, 2.70 eV, was obtained using hybrid functional (HSE06). It is still unknown how to best invoke the correction of the correlation effect for pyrite. Since the local-field and excitonic effects were also omitted in the present calculations, there is room for further studies to achieve better quantitative comparison for positions and intensity ratios of CPs.

V. CONCLUSIONS

The pseudodielectric function $\langle \varepsilon \rangle$ of a natural iron pyrite single crystal has been determined by SE at 77 K. Our $\langle \varepsilon \rangle$ data show a total of six interband CPs. The CP energies were obtained by the standard line-shape analysis, and their electronic origins were identified by DFT calculations and momentum matrix analyses. Our results help to better understand the electronic structure and related optical properties of iron pyrite, which will, in turn, aid in the development of high-performance pyrite solar cells.

*Author to whom correspondence should be addressed: sukgeun.choi@nrel.gov

[1] A. Ennaoui, S. Fiechter, Ch. Pettenkofer, N. Alonso-Vante, K. Büker, M. Bronold, Ch. Höpfner, and H. Tributsch, Sol. Energy Mater, Sol. Cells **29**, 289 (1993).

[2] J. Puthussery, S. Seefeld, N. Berry, M. Gibbs, and M. Law, J. Am. Chem. Soc. **133**, 716 (2011).

[3] C. Wadia, A. P. Alivisatos, and D. M. Kammen, Environ. Sci. Technol. **43**, 2072 (2009).

[4] S. G. Choi, M. van Schilfgaarde, D. E. Aspnes, A. G. Norman, J. M. Olson, T. J. Peshek, and D. H. Levi, Phys. Rev. B **83**, 235210 (2011).

[5] O. E. Semonin, J. M. Luther, S. Choi, H.-Y. Chen, J. Gao, A. J. Nozik, and M. C. Beard, Science **334**, 1530 (2011).

[6]S. Lauer, A. X. Trautwein, and F. E. Harris, Phys. Rev. B **29**, 6774 (1984).

[7]G. U. von Oertzen, R. T. Jones, and A. R. Gerson, Phys. Chem. Miner. **32**, 255 (2005).

[8]V. N. Antonov, L. P. Germash, A. P. Shpak, and A. N. Yaresko, Phys. Status Solidi B **246**, 411 (2009).

[9]L. Vadkhiya and B. L. Ahuja, J. Alloys Compd. **509**, 3042 (2011).

[10]T. A. Bither, R. J. Bouchard, W. H. Cloud, P. C. Donohue, and W. J. Siemons, Inorg. Chem. **7**, 2208 (1968).

[11]A. Schlegel and P. Wachter, J. Phys. C **9**, 3363 (1976).

[12]S. Suga, K. Inoue, M. Taniguchi, S. Shin, M. Seki, K. Sato, and T. Teranishi, J. Phys. Soc. Jpn. **52**, 1848 (1983).

[13]I. J. Ferrer, D. M. Nevskaia, C. de las Heras, and C. Sánchez, Solid State Commun. **74**, 913 (1990).

[14]D. E. Aspnes, in *Handbook of Optical Constants of Solids*, edited by E. D. Palik (Academic, Orlando, 1985), Vol. 1, p. 89.

[15]M. L. Cohen and J. R. Chelikowsky, *Electronic Structure and Optical Properties of Semiconductors*, 2nd ed. (Springer-Verlag, Berlin, 1989).

[16]L. Viña, C. Umbach, M. Cardona, and L. Vodopyanov, Phys. Rev. B **29**, 6752 (1984).

[17]L. Viña, S. Logothetidis, and M. Cardona, Phys. Rev. B **30**, 1979 (1984).

[18]D. E. Aspnes and A. A. Studna, Appl. Phys. Lett. **39**, 316 (1981).

[19]G. Will, J. Lauterjung, H. Schmitz, and E. Hinze, in *Proceedings of the MRS Symposia* (Materials Research Society, Warrendale, PA, 1984), Vol. 22, p. 49.

[20]G. Kresse and J. Furthmüller, Comput. Mater. Sci. **6**, 15 (1996).

[21]G. Kresse and J. Furthmüller, Phys. Rev. B **54**, 11169 (1996).

[22]J. P. Perdew, K. Burke, and M. Ernzerhof, Phys. Rev. Lett. **77**, 3865 (1996).

[23]P. E. Blöchl, Phys. Rev. B **50**, 17953 (1994).

[24]G. Kresse and D. Joubert, Phys. Rev. B **59**, 1758 (1999).

[25]H. J. Monkhorst and J. D. Pack, Phys. Rev. B **13**, 5188 (1976).

[26]P. Bayliss, Am. Mineral. **74**, 1168 (1989).

[27]J. Hu, Y. Zhang, M. Law, and R. Wu, Phys. Rev. B **85**, 085203 (2012). In the present study, the U-correction term was omitted to best fit the experimental spectra.

[28]F. Hulliger and E. Mooser, J. Phys. Chem. Solids **26**, 429 (1965).

[29]M. Gajdos, K. Hummer, G. Kresse, J. Furthmüller, and F. Bechstedt, Phys. Rev. B **73**, 045112 (2006).

[30]M. S. Hybertsen and S. G. Louie, Phys. Rev. B **34**, 5390 (1986).

[31]L. Reining, V. Olevano, A. Rubio, and G. Onida, Phys. Rev. Lett. **88**, 066404 (2002).

[32]C. M. Eggleston, J.-J. Ehrhardt, and W. Stumm, Am. Mineral. **82**, 1036 (1996).

[33]Y. N. Zhang, J. Hu, M. Law, and R. Q. Wu, Phys. Rev. B **85**, 085314 (2012).

[34]M. Cardona, in *Modulation Spectroscopy, Suppl. 11 of Solid State Physics*, edited by F. Seitz, D. Turnbull, and H. Ehrenreich (Academic, New York, 1969), p. 119.

[35]D. E. Aspnes, in *Handbook of Semiconductors*, edited by M. Balkanski (North-Holland, Amsterdam, 1980), Vol. 2, p. 109.

[36]A. Savitzky and M. J. E. Golay, Anal. Chem. **36**, 1627 (1964).

[37]S. Adachi and T. Taguchi, Phys. Rev. B **43**, 9569 (1991).

[38]Y. D. Kim, S. L. Cooper, M. V. Klein, and B. T. Jonker, Phys. Rev. B **49**, 1732 (1994).

[39]P. Lautenschlager, M. Garriga, L. Viña, and M. Cardona, Phys. Rev. B **36**, 4821 (1987).